Fatigue Behavior and Failure Mechanisms of Modified 7075 Aluminum Alloys

J. S. SANTNER AND D. EYLON

The effects of purity level and dispersoid type on the fatigue behavior of 7000 series alloys were investigated. Ten different compositions based on the 7075 alloy were produced with five levels of Fe + Si and either Cr or Zr dispersoids. Notched axial fatigue specimens were tested at room temperature and the fatigue life did not correlate with either purity level or dispersoid type. Specimens failed by three macroscopic modes designated as: slant, vee, or flat fracture. Sectioning analysis showed that the slant, vee, and flat fractures resulted from single, double and multiple initiation, respectively. Both initiation and propagation in all three modes of failures were dominated by slip related fracture on the {111} planes inclined at 35 deg to the tensile axis of the textured material. The same failure mechanisms were observed in smooth fatigue specimens.

ONE approach considered for improving the notched fatigue strength of 2000 and 7000 series aluminum alloys[1] is to reduce the volume fraction of large intermetallic particles such as Cu_2FeAl_7 or Fe_3SiAl_{12}. In particular, the notched fatigue results reported by Reimann and Brisbane,[2] demonstrated that a high purity 7075-T6 alloy had one third greater fatigue strength at 10^6 cycles than a commercial purity 7075-T6. The high purity 7075 had a 0.02 combined wt pct of Fe + Si, while the specifications limits for commercial 7075 purity level is set at a combined wt pct of less than 1.2. The objective of this investigation was to consider in more detail the sensitivity of the notched fatigue strength to the purity of both 7075 aluminum compositions (7X75) heat treated to the peak strength condition (T651). Since the peak hardened temper of 7075 is susceptible to stress corrosion,[3,4] the fatigue tests were conducted in an inert environment to isolate the effect of purity. The T651 heat treatment precipitates η' particles which are shearable by dislocations,[5] and promotes inhomogeneous slip band formation during deformation.[6] Planar slant fracture modes have been reported by several investigators[7-9] in both 2000 and 7000 series aluminum alloys. This fracture morphology and the failure mode are apparently related to inhomogeneous slip band formation.

EXPERIMENTAL

Material and Processing

Ten different compositions based on the 7075 alloy were utilized to study both the effect of purity level (combined wt pct of Fe + Si) and the grain refiner zirconium in place of chromium. The same ten compositions from the same heats were previously used in a work which studied the effect of Fe + Si purity level on the fracture toughness.[10] The experimental compositions are given in Table I along with the composition limits of alloys 7075[11] and 7050[11] for comparison purposes. The 7050 composition is a commercial 7000 series aluminum alloy with the zirconium grain refiner.

The 7X75 specimens were cut from 16 mm (0.625 in.) plate with the tensile axis parallel to the rolling direction. The ingots of each composition in Table I were semicontinuously cast in 100 × 355 mm (4 × 14 in.) molds. Processing of the ingots to the final plate thickness, solution heat treatment, and the T651 heat treatment are given in detail elsewhere.[10,12] The ingots were unidirectionally rolled since cross-rolling was not feasible due to their small size.

The T651 longitudinal average tensile yield strengths are given in Table II for all ten compositions.[12]

Fatigue Testing Procedures

Notched round specimens with $K_t = 3$ were machined according to the geometry given in Fig. 1. To assure that the test results would not be biased by residual

Table I. Composition of Tested Experimental Alloys Compared to Commercial Alloy Compositions

Composition, Wt Pct	Experimental 7X75					
	7075	A	B	C	D	E
Zn	5.1-6.1	5.89	5.91	5.93	5.93	5.94
Mg	2.1-2.9	2.19	2.42	2.39	2.35	2.36
Cu	1.2-2.0	1.50	1.58	1.60	1.64	1.63
Cr	0.18-0.40	0.21	0.22	0.21	0.21	0.21
Fe	0.70	0.02	0.05	0.08	0.13	0.20
Si	0.50	0.01	0.02	0.04	0.06	0.11
Mn	0.30	<0.01	<0.01	<0.01	<0.01	<0.01
Ti	0.20	0.004	0.005	0.012	0.012	0.009
Others (Total)	0.15	<0.01	<0.01	<0.01	<0.01	<0.01
Fe + Si	1.20	0.03	0.07	0.12	0.19	0.31
Composition Wt Pct	Experimental 7X75					
	7050	A-1	B-1	C-1	D-1	E-1
Zn	5.7-6.7	5.73	5.68	5.84	6.02	5.98
Mg	1.9-2.6	2.39	2.39	2.31	2.33	2.45
Cu	2.0-2.8	1.50	1.51	1.54	1.51	1.52
Zr	0.08-0.15	0.12	0.12	0.12	0.12	0.12
Fe	0.15	0.01	0.04	0.08	0.11	0.20
Si	0.12	0.01	0.02	0.04	0.05	0.09
Mn	0.10	<0.01	<0.01	<0.01	<0.01	<0.01
Ti	0.06	0.0004	0.005	0.006	0.005	0.006
Cr	0.04	<0.01	<0.01	<0.01	<0.01	<0.01
Others (Total)	0.10	<0.01	<0.01	<0.01	<0.01	<0.01
Fe + Si	0.27	0.02	0.06	0.12	0.16	0.29

J. S. SANTNER, formerly with the Metals and Ceramics Division, Air Force Materials Laboratory, Wright-Patterson Air Force Base, OH 45433, is now with Inland Steel Corporation Research Laboratory, East Chicago, IN 46312. D. EYLON is with Department of Materials Science and Metallurgical Engineering, University of Cincinnati, Cincinnati, OH 45221.

Manuscript submitted December 15, 1978.

ISSN 0360-2133/79/0711-0841$00.75/0

stresses introduced during machining, low stress grinding conditions were used.[13] Fatigue tests were performed in a 2 ton (17.8 KN) Schenek machine with completely reversed axial loading ($R = -1$). A number of supplemental tests were run in a tension/tension mode ($R = +0.1$) to preserve the fracture topography for mechanism studies. Because of the inherently large scatter in high cycle fatigue tests[14] and the long test time involved, all specimens were tested at only two stress levels. In this manner, enough fatigue life (N_f) data was produced within the scope of the program to establish statistically significant trends rather than generating an entire S-N curve for all ten compositions. To isolate the notched fatigue behavior from the corrosion fatigue cracking,[3,4] the specimens were tested in an inert environment. The specimen gage section was immersed in a low sulfur vacuum pump oil during testing to minimize the deleterious effect of ambient water vapor and provide a standard test environment.

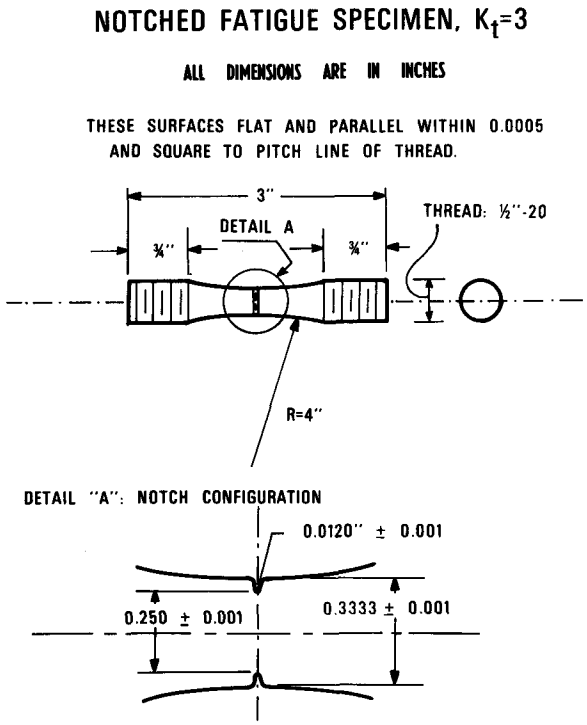

Fig. 1–Notched fatigue specimen geometry. Machining dimensions are in inches.

Table II. Average T651 Longitudinal Yield Strength of the Ten Experimental Compositions

Composition	Fe + Si Content, Wt Pct	0.2 Pct Offset Yield Strength MPa	(KSI)
A	0.03	503	(73.0)
B	0.07	509	(73.8)
C	0.12	518	(75.1)
D	0.19	501	(72.6)
E	0.31	475	(68.8)
A-1	0.02	534	(77.4)
B-1	0.06	512	(74.2)
C-1	0.12	525	(76.1)
D-1	0.16	550	(79.7)
E-1	0.29	548	(79.5)

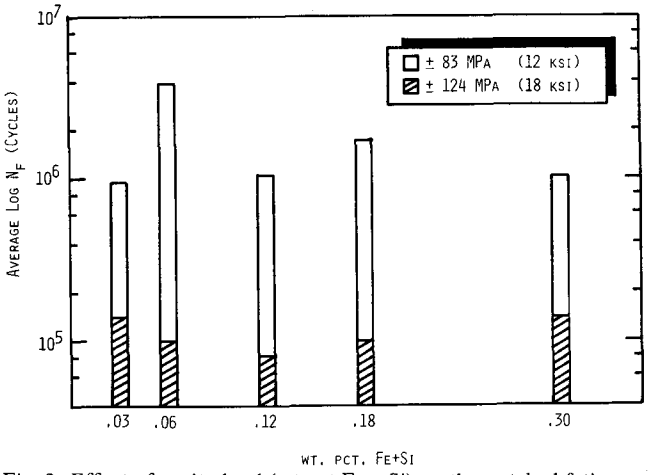

Fig. 2–Effect of purity level (wt pct Fe + Si) on the notched fatigue life for specimens cycled at $R = -1$ in an inert oil environment.

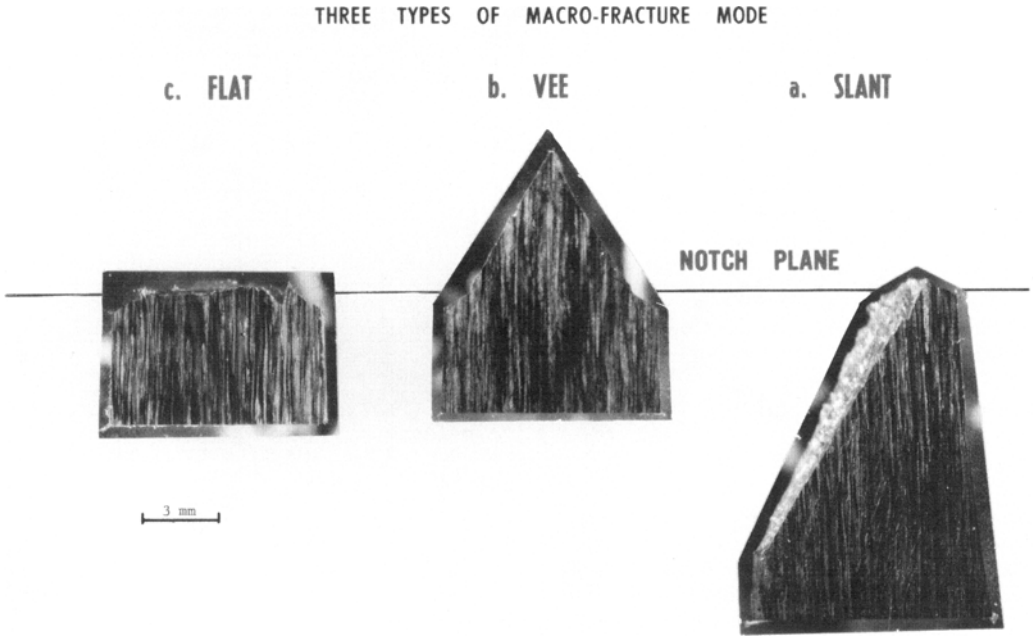

Fig. 3–Three types of macrofracture mode: (*a*) slant fracture, (*b*) vee fracture, and (*c*) flat fracture.

Fractography, Precision Sectioning and TEM

All fatigue fracture surfaces were examined by optical stereoscope and scanning electron microscopy (SEM). The fatigue crack initiation sites were located, and the morphologies of both the fatigue fracture and the overload fracture surfaces were characterized.

To enable the identification of the crack initiation and propagation mechanisms, the specimens were sectioned through the initiation site in a plane perpen-

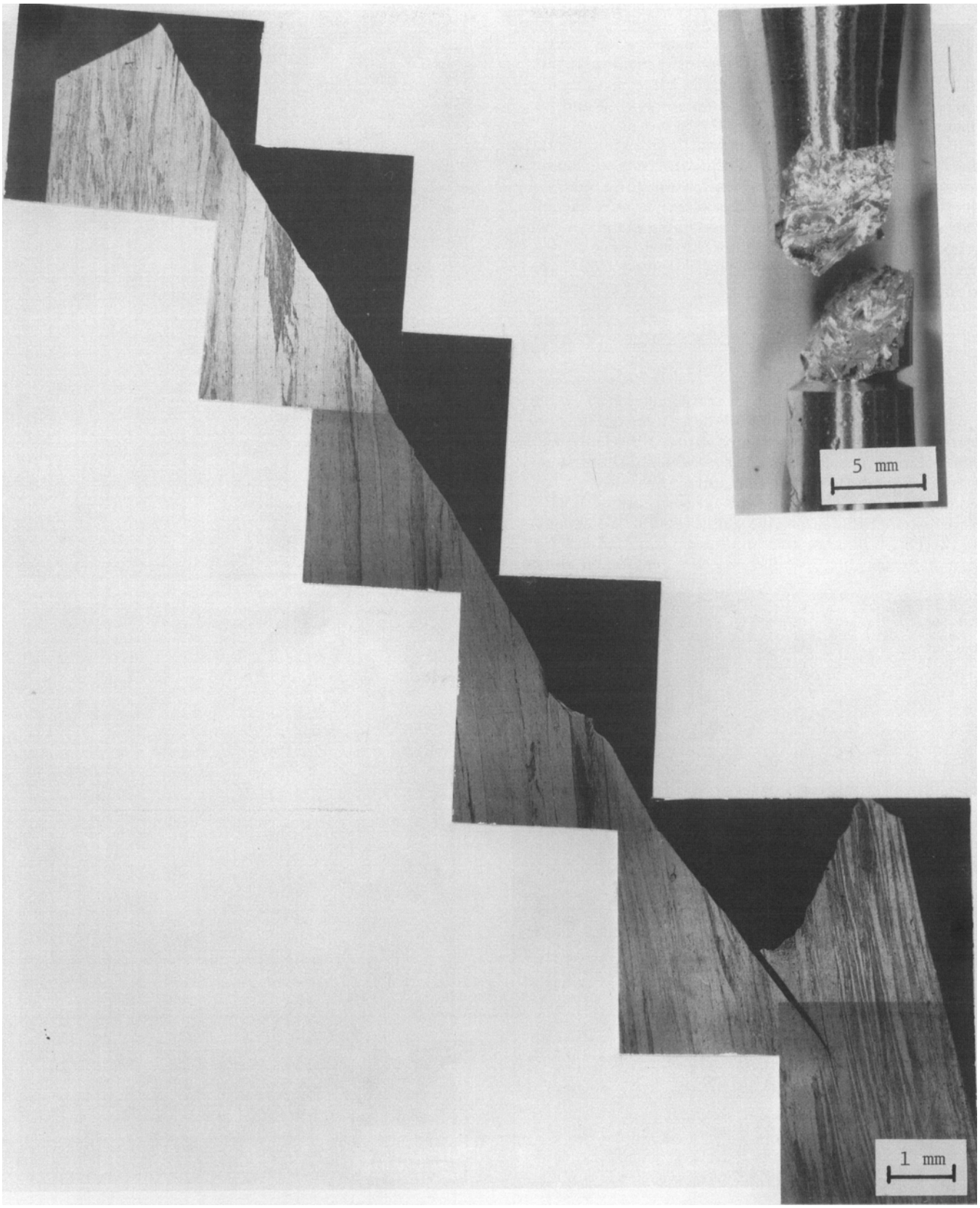

Fig. 4—Fatigue initiation, propagation, and final overload fracture in a notched specimen as viewed in a cross-section through the center plane perpendicular to the planar fracture surface.

dicular to the fracture surface and parallel to the specimen axis. The precision sectioning technique employed here was described in detail elsewhere.[15] The sectioned plane was then metallographically mounted, polished and etched using standard metallographic techniques for aluminum alloys. After the microstructure underlying the initiation and propagation locations was optically characterized, the mount material was dissolved. SEM examination of the tilted specimen revealed both a segment of the fracture area and its underlying microstructure on the same image.

To identify the specimen crystallographic orientation and to characterize the microdeformation mechanisms, the sectioned samples were wafered parallel to the section plane and transmission electron microscopy (TEM) specimens were prepared using standard electropolishing techniques.[16] This allowed correlations of the metallographic observations on the section plane with TEM observations.

RESULTS AND DISCUSSION

Notched Fatigue Life

Notched fatigue life tests were conducted at two different stress levels to establish the average notched fatigue lives for the ten compositions. Variance analysis at the 95 pct confidence level showed there is no effect of dispersoid type (chromium bearing *vs* zirconium bearing alloys) on the notched fatigue life. Since almost the same five purity levels are present in the chromium bearing and the zirconium bearing compositions, both populations were combined as one to establish the effect of purity level on the notched fatigue life. These results are depicted on the bar graph in Fig. 2. Each bar is the average of ten notched fatigue tests, five for the chromium bearing alloys and

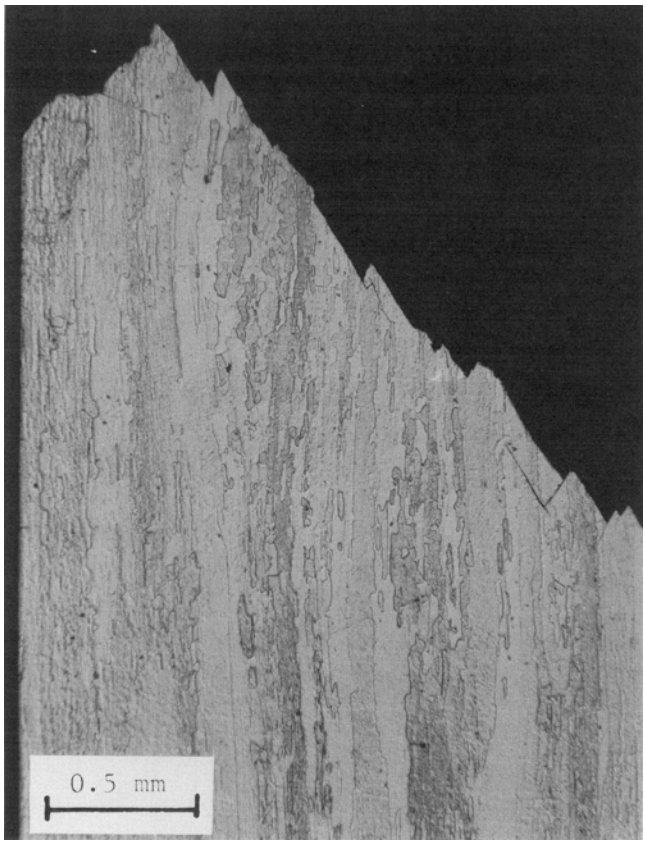

Fig. 5–Fatigue initiation and propagation in a fractured smooth specimen which failed by slant mode as viewed in a cross-section through the center plane perpendicular to the planar fracture surface.

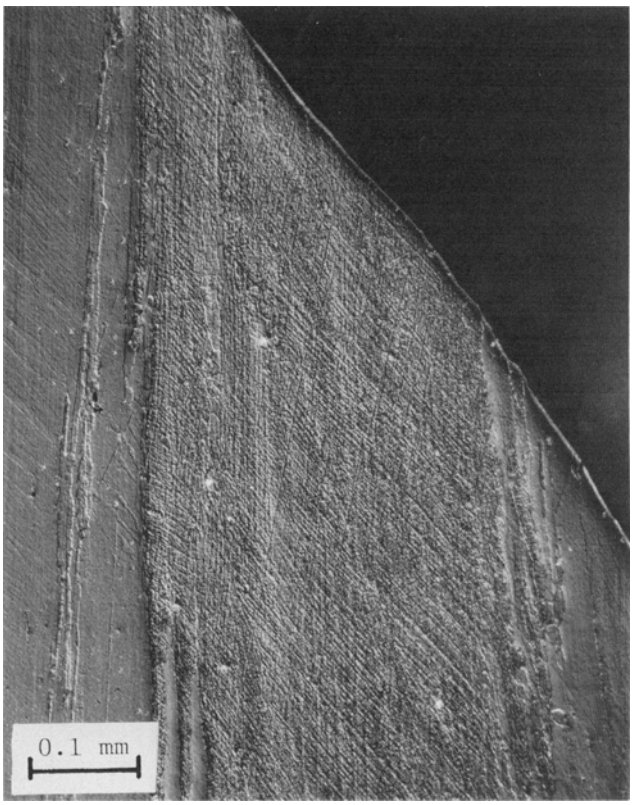

(*a*)

(*b*)

Fig. 6–Slip band formation directly below the fracture surface: (*a*) in a notched specimen and (*b*) in a smooth specimen. Note that the slip lines are parallel to the fracture surface.

five for the zirconium bearing alloys at each purity level and load level tested. The analysis of variance showed the notched fatigue lives are statistically different, but there is no clear trend of increased life with increased purity level (lower combined wt pct of Fe + Si). There is also no correlation between the fatigue lives and the T651 tensile yield strength levels (Table II) of the ten compositions. The lack of a monotonic relationship suggests that purity by itself is not the fundamental metallurgical variable controlling the notched fatigue life.

Fatigue Fracture Modes

The initial low magnification observations revealed that the fractures of all compositions can be divided into three categories. The first one, which is also the least frequently observed is the *slant fracture* (Fig. 3(*a*)). In this mode, the crack has initiated in the notch area on a plane inclined at approximately 35 deg to the tensile axis. It is then propagated away from the notch plane and failed on the same 35 deg inclined fracture plane.

The second category is the *vee fracture* (Fig. 3(*b*)). In this mode, two cracks initiated in the notch area and propagated, on opposing planes, each inclined at approximately 35 deg to the tensile axis. The resulting fracture surfaces resemble a chisel point edge.

The third type of fracture appeared to be a *flat fracture* at low magnification (Fig. 3(*c*)). However, as will be discussed later, higher magnification observations show that this fracture was composed of slanted segments on the order of the grain width. No correlation exists between the three fracture modes and any of the experimental parameters (composition, stress level, and R ratio), or the fatigue lives.

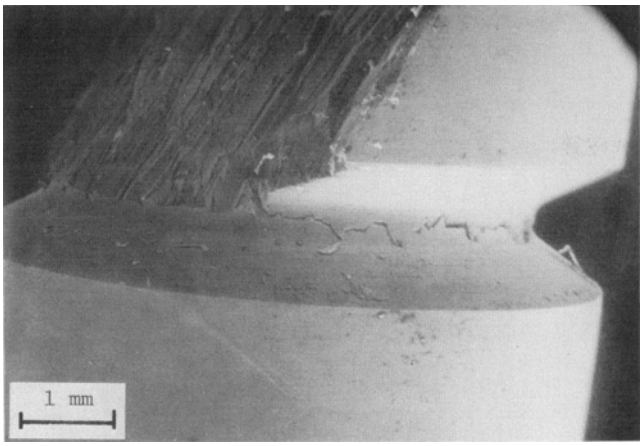

Fig. 7—Multiple initiation in the notched area of a specimen which failed by the slant fracture mode.

Micromechanisms of Slant Fracture

A composite picture of the slant fracture section (Fig. 4) shows that initiation, propagation and overload fracture occurred almost on the same plane. It should be noted that in this figure, the fracture plane is perpendicular to the section plane (*i.e.*, the picture plane). The inset shows the fracture surfaces before sectioning. To determine if this mode of failure is found exclusively in notched specimens, smooth fatigue specimens were machined from composition A-1 tested with the same cyclic stress. All three fracture modes were also observed in these specimens. Figure 5 is an example of a slant fracture in a smooth fatigue specimen.

Higher magnification photomicrographs from the vicinity of the fracture surface (Fig. 6), show intense slip bands parallel to the fracture surface. This indicates that the fracture plane is related to the inhomogeneous planar slip bands. A SEM investigation was conducted to identify these slip planes. The planar fracture throughout the specimen, as evidenced in Figs. 4 and 5, indicates that the undirectional rolling introduced strong crystallographic texturing.

The SEM image of the notch area in a slant fracture specimen (Fig. 7) shows that the notch provides many initiation locations. In the case of the slant fracture only one initiation location developed to a full size crack. The vee shaped failures are the result of two opposing initiation sites. A high magnification view of the flat fracture (Fig. 8) shows that the apparent flat appearance at low magnification is made of many slanted segments which are also inclined at approximately 35 deg to the tensile axis.

The slant fracture mode with the same 35 deg inclination dominates all three categories and suggests that in all three cases, the failure was controlled by the same mechanism. The only difference in the macroscopic appearance (Fig. 3) is the number of active initiation sites: *one* site in the *slant* category, *two* sites in the *vee* category, and *multiple* initiations in the *flat* category. At this point, it is not clear what causes the differences in the initiation behavior.

Trace analysis of the TEM photomicrograph (Fig. 9(*a*)) on a plane parallel to the section plane in Fig 6,

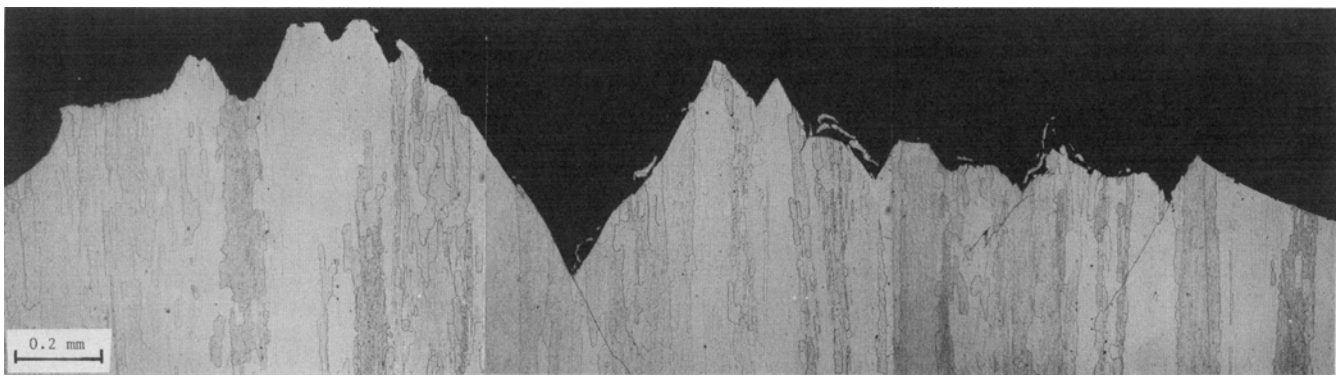

Fig. 8—Fatigue initiation, propagation, and final overload fracture in a notched specimen which failed by the flat fracture mode as viewed in a cross-section through the center plane perpendicular to the planar fracture facets.

clearly shows slip on {111} planes. The zone axis of the corresponding diffraction pattern identified the section plane as {110} plane. The photomicrograph in Fig. 9(*b*) shows intense shear progressing from one grain to another on the same plane which is an indication of crystallographic texture.

Some locations on the section planes revealed secondary crystallographic fractures parallel to the fracture surface (Fig. 10(*a*)). Since the section plane in all specimens sliced perpendicular to the slant fracture plane and parallel to the specimen axis was identified by TEM analysis to be {110} plane, it was possible to perform single surface trace analysis. The (110) stereographic projection in Fig. 10(*b*) identifies and

(*a*)

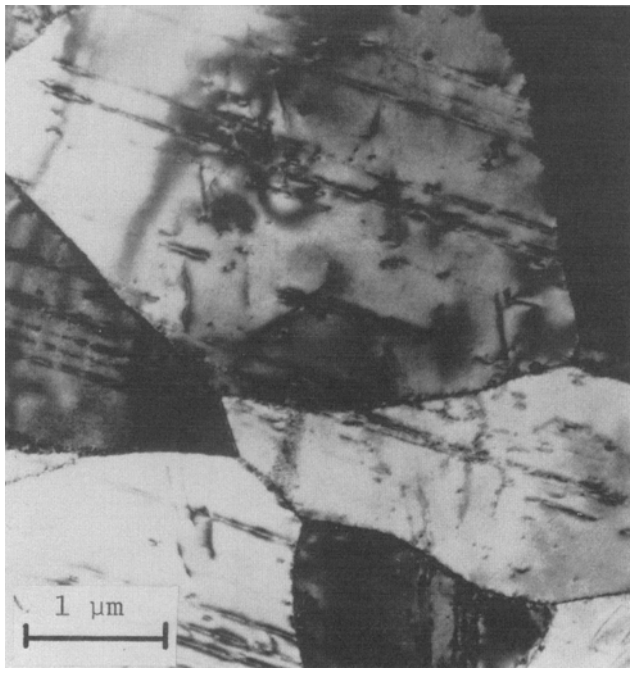

(*b*)

Fig. 9—Transmission electron micrographs of thin foils taken from the sectioned plane shown in Fig. 4: (*a*) oriented to show the {111} slip planes in an edge on position, and (*b*) penetration of a {111} type slip across grain boundaries.

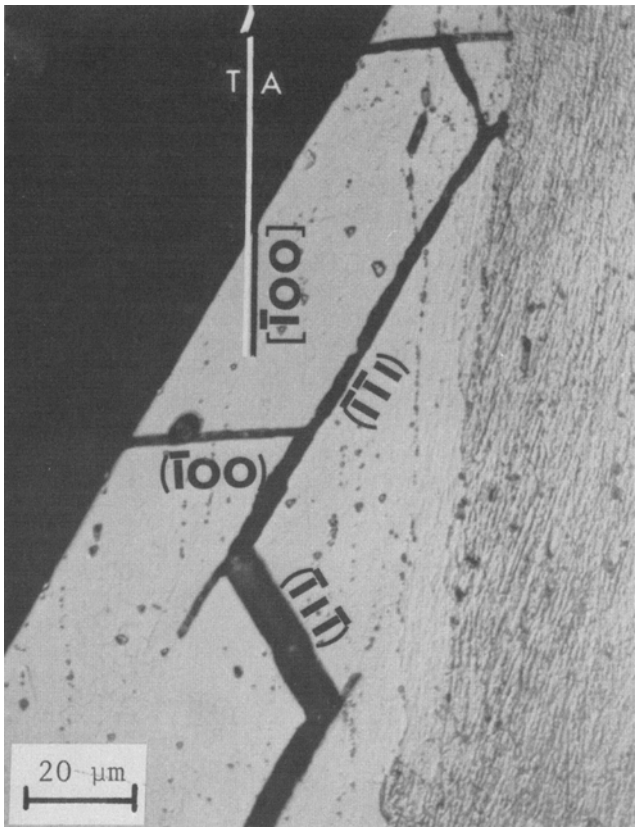

(*a*)

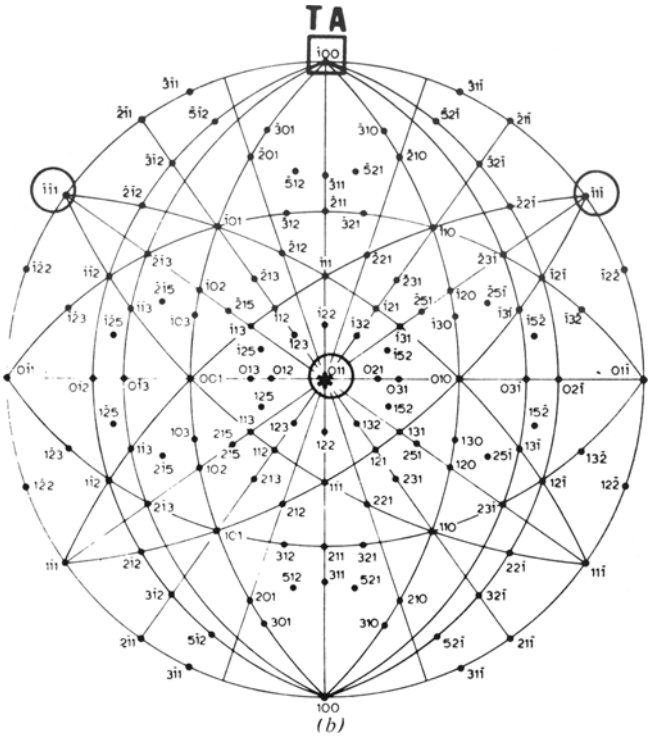

(*b*)

Fig. 10—Photomicrograph of the cross-section plane relating the slip observed in Fig. 9(*a*) to: (*a*) primary and secondary slant fractures and their orientations as indicated on (*b*) standard (001) stereographic projection.

indexes the primary and secondary slant fracture planes in Fig. 10(*a*), assuming that they are in an edge-on position. Therefore, the slant fracture, which is perpendicular to the sectioned plane is parallel to the $(\bar{1}\bar{1}1)$ crystallographic plane. This also provides the correct angular relationship for the $\{111\}$ crystallographic planes to be inclined at 35 deg from the tensile axis as in the inclined fracture facets.

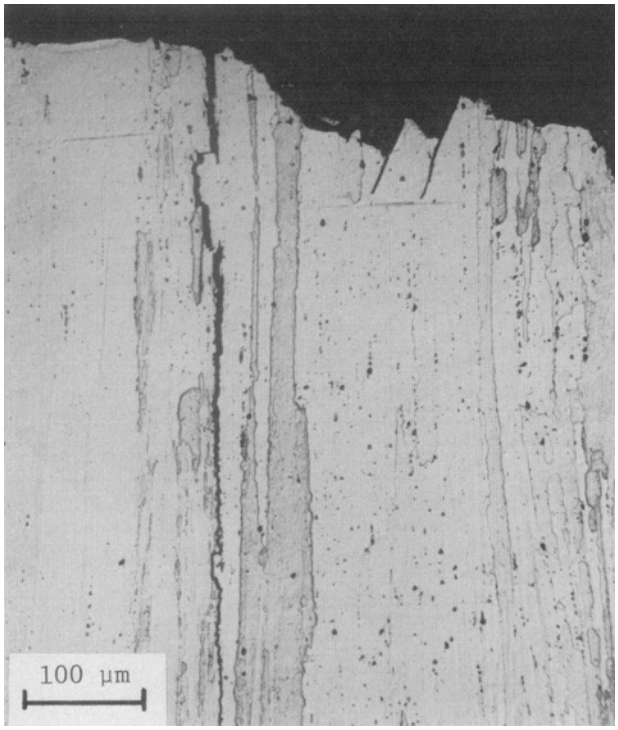

(*a*)

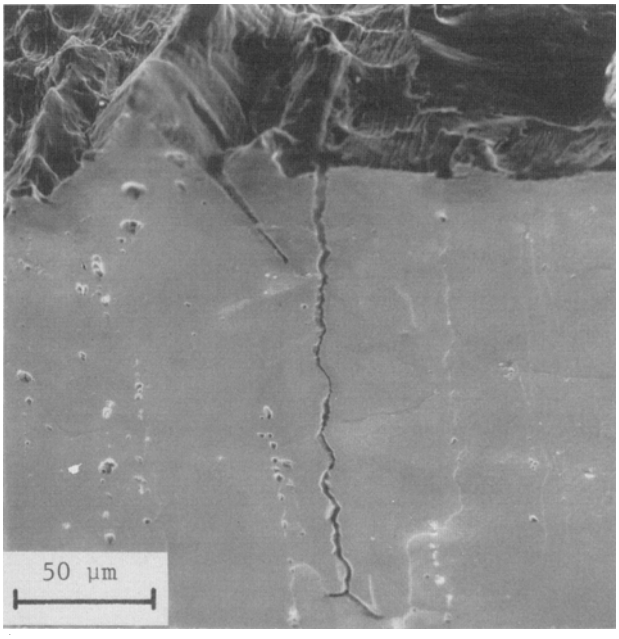

(*b*)

Fig. 11—Secondary cracking parallel to the tensile axis in a high ΔK region: (*a*) photomicrograph of grain boundary cracking, (*b*) scanning electron micrograph showing the grain boundary cracking in both the microstructure and on the fracture surface, and (*c*) matching of striations across a grain boundary crack.

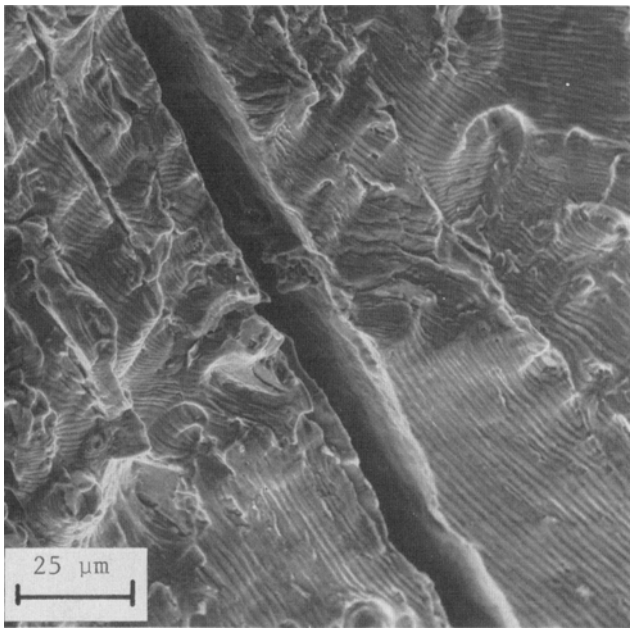

(*c*)

Secondary Cracking

The secondary cracking in the flat fracture category specimens along the grain boundaries (shown on the section plane in Fig. 11(*a*)) is a puzzling feature since these cracks propagate parallel to the tensile axis. Figure 11(*b*) shows the fractographic/microstructural relationship for this type of secondary cracking. Figure 11(*c*) shows fatigue striations which follow continuously across a secondary crack. This indicates that the secondary intergranular cracking developed after the main crack advanced through this area; otherwise, the striations will not be continuous as shown in Fig. 11(*c*). As the crack propagates through the specimen, it creates loading eccentricities and subsequent bending moments that can cause cracking parallel to the tensile axis.

SUMMARY AND CONCLUSIONS

The effect of Fe + Si purity level and dispersoid type on the fatigue behavior of ten 7X75 aluminum compositions was studied in an attempt to improve the notched fatigue life.

1) The notched fatigue life did not correlate with either dispersoid type (chromium bearing *vs* zirconium bearing alloys) or purity level.

2) No correlation between the tensile yield strength and the notch fatigue life was observed.

3) Specimens failed by three macroscopic modes that are designated as: slant, vee and flat fracture.

4) There is no correlation between the mode of crack initiation and the fatigue life for all the experimental variables (composition, stress level, and R ratio).

5) Precision sectioning analysis shows that the slant, vee, and flat fractures are the result of single, double, and multiple initiation, respectively.

6) Axial smooth fatigue specimens also exhibit the same three macroscopic modes of failure.

7) Trace Analysis by TEM verifies both $\{111\}$ slip and texture in the tested 7X75 plates.

8) In all three failure modes, fracture facets are

dominated by a slip related fracture. The slip and the fracture are inclined at 35 deg to the tensile axis and are identified to be on {111} planes.

9) Intergranular secondary cracks which are parallel to the tensile axis, probably developed after the main crack propagated past the grain boundary.

ACKNOWLEDGMENTS

The authors wish to acknowledge Messers. Charles Smith and Anthony Houston (University of Cincinnati) for their help in the testing and metallography. Messers, Ralph E. Omlor and Brewster Strope (SRL) are acknowledged for their assistance in the electron microscopy analysis. Advice on the statistical analysis of the data was provided by Mr. J. F. Santner (USEPA). Discussions with Mr. Walter M. Griffith (AFML) are appreciated. A portion of this work was done under USAF Contract No. F-33615-76-C-5227.

REFERENCES

*1. D. L. Thompson and R. E. Zinkham: Technical Report AFML-TR-75-247, vol. II, Air Force Materials Laboratory, September 1974.
2. W. H. Reimann and A. W. Brisbane: *Eng. Fract. Mech.*, 1973, vol. 5, pp. 67-78.
3. L. F. Mondolfo: *Met. Mater.*, 1971, vol. 5, p. 95.
4. F. G. Ostermann and W. H. Reimann: ASTM STP 467, p. 16, Philadelphia, Pa., 1970.
*5. A. W. Somer, N. E. Paton, and D. G. Folgner: Technical Report AFML-TR-72-5, Air Force Materials Laboratory, February 1972.
6. J. G. Byrne, M. E. Fine, and H. Kelly: *Phil. Mag.*, 1961, vol. 6, pp. 1119-45.
†7. H. -J. Dudek: *Deutsch Luft-und Raumfahrt Forschungsbericht*, (DLR-Research Report), DLR-FB 73-100, 1973.
8. J. Schijve: Report LR-240, Department of Aerospace Engineering, Delft University of Technology, January 1977.
9. J. Schijve: *Eng. Fract. Mech.*, 1978, vol. 10, pp. 359-70.
10. J. S. Santner: *Met. Trans. A*, 1978, vol. 9A, pp. 769-79.
*11. *Aerospace Structural Metals Handbook*, AFML-TR-68-115, Air Force Materials Laboratory, 1975.
*12. P. J. Blau: Technical Report AFML-TR-75-140, Air Force Materials Laboratory, October 1975.
*13. *Surface Integrity of Machined Materials*, Technical Report AFML-TR-74-60, Air Force Materials Laboratory, April 1974.
14. A. S. Tetelman and A. J. McEvily, Jr.: *Fracture of Structural Materials*, John Wiley and Sons, New York, 1967.
15. W. R. Kerr, D. Eylon, and J. A. Hall: *Met. Trans. A*, 1976, vol. 7A, pp. 1477-80.
16. G. Thomas: *Transmission Electron Microscopy of Metals*, John Wiley and Sons, New York, 1966.

*Available through NTIS, 5285 Port Royal Rd., Springfield VA. 22161.
†Available through DFVLR, Wissenschaftliches Berichtswesen der DFVLR, Postfach 90 60 68, 5000 Köln 90, W. Germany.